Article

Structure and transformation of bacteriophage A511 baseplate and tail upon infection of *Listeria* cells

Ricardo C Guerrero-Ferreira[1,†] (iD), Mario Hupfeld[2], Sergey Nazarov[1,‡], Nicholas MI Taylor[1,§] (iD), Mikhail M Shneider[1,3] (iD), Jagan M Obbineni[4,5], Martin J Loessner[2], Takashi Ishikawa[4], Jochen Klumpp[2,*] (iD) & Petr G Leiman[1,¶,**] (iD)

Abstract

Contractile injection systems (bacteriophage tails, type VI secretions system, R-type pyocins, etc.) utilize a rigid tube/contractile sheath assembly for breaching the envelope of bacterial and eukaryotic cells. Among contractile injection systems, bacteriophages that infect Gram-positive bacteria represent the least understood members. Here, we describe the structure of *Listeria* bacteriophage A511 tail in its pre- and post-host attachment states (extended and contracted, respectively) using cryo-electron microscopy, cryo-electron tomography, and X-ray crystallography. We show that the structure of the tube-baseplate complex of A511 is similar to that of phage T4, but the A511 baseplate is decorated with different receptor-binding proteins, which undergo a large structural transformation upon host attachment and switch the symmetry of the baseplate-tail fiber assembly from threefold to sixfold. For the first time under native conditions, we show that contraction of the phage tail sheath assembly starts at the baseplate and propagates through the sheath in a domino-like motion.

Introduction

A511 is a lytic bacteriophage that infects almost all strains of *Listeria monocytogenes* and *L. ivanovii* (Zink & Loessner, 1992; Klumpp *et al*, 2008; Habann *et al*, 2014). It belongs to the subfamily *Spounavirinae* which also includes phages SPO1 (Stewart *et al*, 2009), Twort (Kwan *et al*, 2005), ISP (Vandersteegen *et al*, 2011), LP65 (Chibani-Chennoufi *et al*, 2004), and many others (Klumpp *et al*, 2010). These viruses have a similar genome organization, and despite their host diversity (*Bacillus, Staphylococcus, Lactobacillus, Enterococcus,* and other Gram-positive bacteria), their virion proteins display high similarity at the amino acid level (e.g., the capsid proteins have greater than 60% sequence identity; Habann *et al*, 2014). Many of these viruses are used as tools in biotechnology, e.g., bacterial typing (Loessner, 1991; van der Mee-Marquet *et al*, 1997), detection (Loessner *et al*, 1996; Hagens *et al*, 2011), and elimination (Guenther *et al*, 2009), as well as in medical applications, e.g., elimination of staphylococcal infections (Vandersteegen *et al*, 2011; Kazmierczak *et al*, 2014). However, the mechanism by which these viruses recognize and attach to their host cells remains poorly understood.

Bioinformatic analysis shows that tail assembly proteins of A511 are encoded by a continuous cluster of genes *93* through *109* (Habann *et al*, 2014). The baseplate and tail fiber/receptor-binding protein genes are downstream from the tail sheath and tail tube genes *93* and *94*, respectively. In this aspect, the organization of the A511 tail gene cluster and the amino acid sequences of its tail proteins are both similar to the so-called "simple" contractile tail phages, e.g., Mu, P2, in which the baseplate is composed of small

---

1 Laboratory of Structural Biology and Biophysics, School of Basic Sciences, École Polytechnique Fédérale de Lausanne, Lausanne, Switzerland
2 Institute of Food, Nutrition and Health, ETH Zurich, Zurich, Switzerland
3 Shemyakin-Ovchinnikov Institute of Bioorganic Chemistry, Laboratory of Molecular Bioengineering, Moscow, Russia
4 Laboratory of Biomolecular Research, Paul Scherrer Institute, Villigen PSI, Switzerland
5 Centre for Agricultural Innovations and Advanced Learning (VAIAL), Vellore Institute of Technology, Vellore, India
*Corresponding author. Tel: +41 446323855; E-mail: jochen.klumpp@hest.ethz.ch
**Corresponding author. Tel: +1 832 908 6635; E-mail: pgleiman@utmb.edu
†Present address: Center for Cellular Imaging and NanoAnalytics (C-CINA), Biozentrum University of Basel, Basel, Switzerland
‡Present address: Focal Area Infection Biology, Biozentrum University of Basel, Basel, Switzerland
§Present address: Structural Biology of Molecular Machines Group, Protein Structure & Function Programme, Novo Nordisk Foundation Center for Protein Research, Faculty of Health and Medical Sciences, University of Copenhagen, Copenhagen, Denmark
¶Present address: Department of Biochemistry and Molecular Biology, Sealy Center for Structural Biology and Molecular Biophysics, University of Texas Medical Branch, Galveston, TX, USA

---

proteins and the corresponding genes display synteny (Buttner *et al*, 2016). The A511 baseplate undergoes a major structural transformation upon sheath contraction (Habann *et al*, 2014) although the details of this process remain unclear. Recently, Novacek *et al* (2016) reported a cryo-electron microscopy (cryoEM) study of the structure of phage phi812, an A511 relative that infects *Staphylococcus aureus*. However, the baseplate cryoEM map was of insufficient quality to identify the location of component proteins.

Here, we show that the baseplate-tail fiber complex of A511 is threefold symmetric in the extended state of the tail and switches to be nearly sixfold symmetric in the contracted state. We assign electron densities to all baseplate proteins and visualize the transformation of the baseplate upon host cell binding. We also report the crystal structure of A511 gene product 105 (gp105), which greatly helped with the interpretation of the cryoEM density. Finally, we captured the A511 particle in a partially contracted state with the baseplate attached to the *Listeria* cell wall, the baseplate-proximal part of the sheath in the contracted state and the distal part still in the extended state. This observation demonstrates that host cell-binding associated changes in the baseplate structure trigger sheath contraction, which then propagates through the sheath as a wave. Several elements of this complex process were observed earlier using phage particles in which the contraction was triggered by a non-physiological treatment of the sample (urea, high temperature, low pH, etc.) which was then fixed and stained with heavy atom salts, but to our knowledge no other report showed the process in its entirety and in near-native conditions for any contractile tail bacteriophage (Eiserling, 1967; Simon & Anderson, 1967a,b; Donelli *et al*, 1972; Benz & Goldberg, 1973; Moody, 1973).

Table 1. Data collection and processing statistics for single particle image reconstruction of A511 baseplate.

	Extended tails (Pre-attachment)	Spontaneously contracted tails (Post-attachment)	Urea-contracted tails (Post-attachment)
Number of initial micrographs	3,975		2,221
Micrographs after CTF screening	3,127		2,221
Number of particles extracted	14,438	2,234	10,122
Particles after 2D alignment and classification	13,334	2,209	9,218
After 3D classification	11,331	1,853	9,218
Resolution after 3D refinement (Å)	16	18	16
Resolution after post-processing (Å)	14	16	14
EMDB accession code	EMD-7560	EMD-7561	EMD-7559

Results and Discussion

CryoEM photographs of freshly prepared A511 sample showed that about 13% of particles had contracted tails (Table 1, Fig EV1A) indicating that the A511 tail is a metastable structure that can spontaneously contract resulting in a post-host cell attachment conformation, a property it shares with other contractile systems (Leiman & Shneider, 2012; Brackmann *et al*, 2018). Borrowing from the T4 phage system (Leiman *et al*, 2004; Fokine *et al*, 2013), we used urea to switch all particles to the contracted tail state. We then employed the single particle cryoEM image reconstruction procedure (Cheng *et al*, 2015) to analyze the structure of the baseplate and the baseplate-proximal part of the A511 sheath in the pre-host attachment extended state (Fig 1A, D and F), in the post-host attachment spontaneously contracted state (Fig 1B, E and H), and in the urea-induced contracted state (Fig 1C, F and I). The corresponding cryoEM maps have resolutions of 14 Å, 16 Å, and 14 Å, respectively (Table 1). We have also studied the transformation of the structure of the A511 particle upon binding to *Listeria* cell wall surface with the help of cryo-electron tomography (cryoET).

The composition and structure of the A511 baseplate is similar to that of T4

The resolution of the A511 cryoEM maps did not allow for *ab initio* segmentation of the electron density into the component proteins. Bioinformatic analysis that employs structure-based hidden Markov's

model (HMM) profiles (Table 2) showed that most A511 tail proteins or their domains have orthologs in the well-studied phage T4 for which the atomic structure of the tube-baseplate complex is available (Taylor *et al*, 2016). However, many T4 tail proteins are larger than their A511 counterparts and the use of the T4 baseplate structure in the interpretation of A511 cryoEM maps required removing some parts of the model. We trimmed the T4 tail tube-baseplate structure to leave the domains that have definitive orthologs in the A511 tail (Table 2). This structure matched the conserved "tube-baseplate core complex", which was proposed to be present in most contractile injection systems and which was described in our earlier studies (Taylor *et al*, 2016, 2018). It consists of the tube protein (T4 gp19 and gp54), baseplate hub protein 1 (BH1, gp48), baseplate hub 2 (BH2, gp27), baseplate spike (BS, gp5), and four baseplate wedge proteins (BW1, BW2, BW3 and BW4—gp25, gp6, gp7, and gp53, respectively, although only some domains of gp6, gp7, and gp53 are conserved). Only a small part of T4 BW4 gp53 protein, namely, a LysM-like domain (Maxwell *et al*, 2013), is conserved in A511 (residues 4–41 of BW1 gp102 are predicted to form a LysM domain). The small size and lower degree of conservation make placement of the LysM domain of the BW1 gp102 protein into the 14 Å resolution A511 cryoEM map uncertain. We, therefore, removed this protein from the T4-based model of the universally conserved tube-baseplate core complex.

The conserved tube-baseplate core complex of T4 was then fitted as a rigid body into the A511 extended tail cryoEM map with the
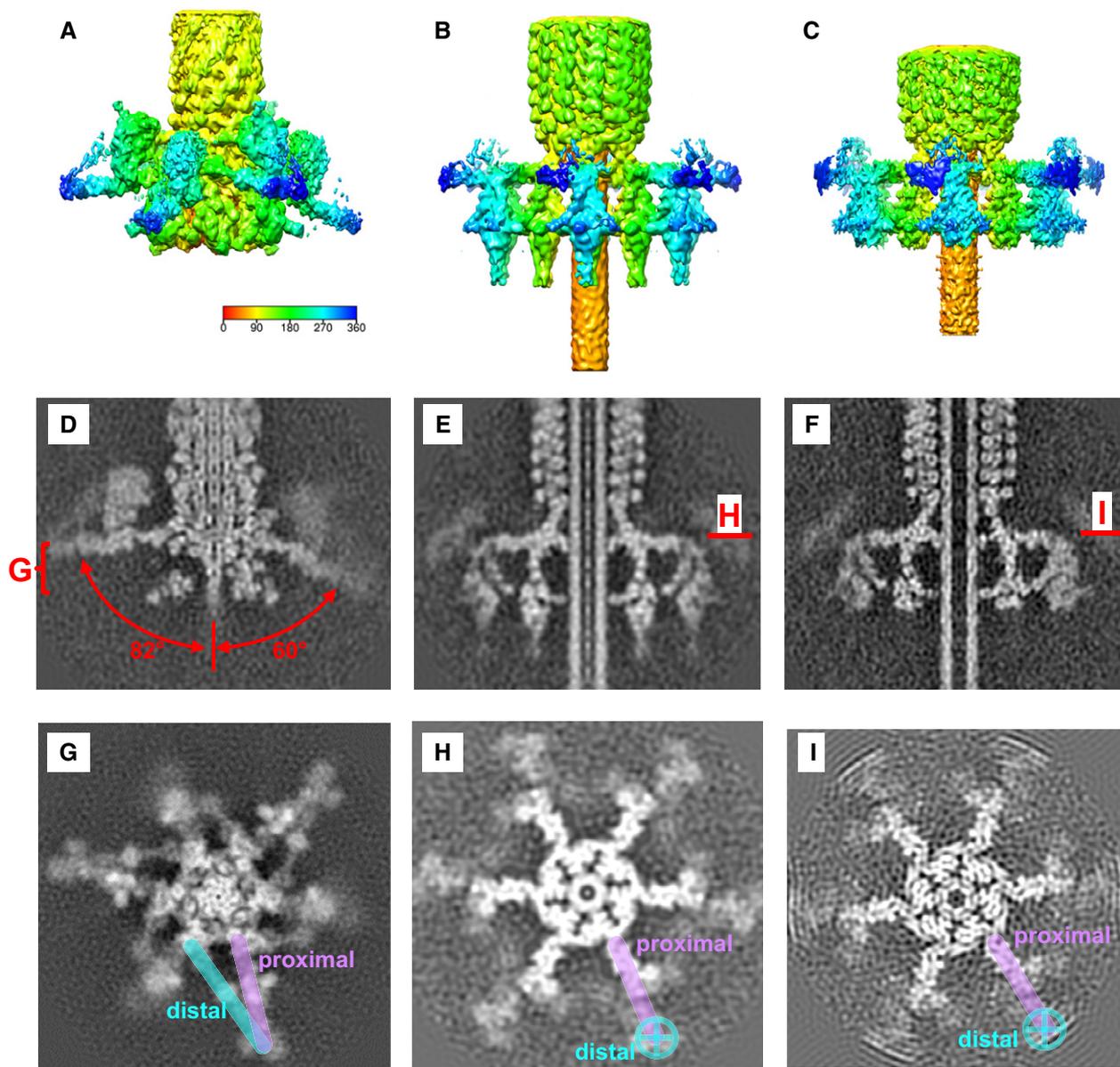
Figure 1. CryoEM reconstructions of the baseplate region of the A511 tail in the pre- and post-host cell attachment states.

A–C CryoEM reconstructions of the extended, spontaneously contracted, and urea-contracted tails colored according to the distance to the axis of the reconstruction. The color code bar shown in panel (A) and which is given in Angstroms is the same for all the three panels.

D–F The central axial sections of the reconstructions. Note the C-terminal domain of gp104 and other low-density features that do not visualize well in the isosurface representation [panels (A–C)]. Letters G, H, and I indicate the position of the cross sections shown in the homonymously labeled panels below.

G A 69 Å-thick slice of the reconstruction of the extended sheath cryoEM map orthogonal to the sixfold axis. The proximal and distal parts of one of the three fibers that run at 82° to the sixfold axis are indicated with a semitransparent cyan and magenta lines, respectively.

H, I Sections of the spontaneously and urea-contracted sheath structures that cut through the baseplate/proximal part of the fiber plane, whose position in the reconstructions is indicated with a red line in panels (E and F). The putative direction of the distal part of the fiber, which is completely disordered in the reconstructions, is indicated with a solar cross symbol.

help of the automatic rigid body fit algorithms as implemented in the graphics programs Coot (Emsley *et al*, 2010) and UCSF Chimera (Pettersen *et al*, 2004) (Fig 2, Table 3). We also split this structure into two parts—the central tube/spike complex and the baseplate core—and fitted them separately with the help of the Coot and UCSF Chimera rigid body fit procedures. The resulting composite structure

was essentially the same as the one comprising one rigid body (Table 3). This shows that neither of the two components dominates the overall fitting procedure and indirectly confirms the validity of such interpretation.

The A511 cryoEM map agrees with the conserved core part of the T4 baseplate-tube structure remarkably well (Table 3, e.g.,

Table 2.   Putative functions and their acronyms of tail-associated genes of A511.

Gene name	Length of gene product, a.a.	Function (acronym), additional functional details	T4 or other phage ortholog	PDB (with chain ID) and/or PFAM code of best match	Residue range of A511 protein	Residue range of best match	E-value
93	562	Sheath	Gp18	3HXL	1–545	1–427	2.8e-44
				3LML	2–559	3–455	2.1e-43
				3J9Q	12–540	3–359	7e-25
				5LI2	1–562	1–587	4.0E-65
94	140	Tube	Gp19, gp54, gp3	2GUJ	2–133	1–134	0.0066
				4W64	8–132	4–133	1.9
95	147	Tape Measure Chaperone (TMC), putative	Gp28 (putative)				
96	197	Unknown, possible assembly chaperone (α-helical)	Unknown				
97	1,242	Tape Measure Protein (TMP)	Gp29	COG3941	230–865	10–586	0.002
98	795	Baseplate Hub 2 (BH2)	Gp27	3D37	1–586	1–337	0.0042
				1WRU	38–516	16–267	0.0096
				3CDD	18–555	4–310	0.024
			Peptidoglycan endopeptidase (gp5 lysozyme domain)	4Q4G	624–794	320–472	7.8E-13
99	510	Baseplate Spike (BS)	Gp5	2Z6B	26–256	4–205	0.028
				4MTK	29–121	364–454	0.08
				4RU3	27–106	30–104	0.078
100	237	Baseplate Hub 1 (BH1), tube basal disk	Gp48	PF06995	22–150	1–120	0.51
				COG3499	22–161	6–136	0.13
101	177	Unknown, possible assembly chaperone (α-helical)	Unknown				
102	236	Baseplate Wedge 1 (BW1), tail sheath-baseplate attachment	Gp25	5IV5_DG	115–231	11–131	1.4E-13
		Baseplate Wedge 4 (BW4), baseplate core bundle clamp	Gp53	5IV5_V	4–41	45–82	0.97
103	348	Baseplate Wedge 2 (BW2), baseplate circularization	Gp6	3H2T	187–323	1–151	1.1E-8
				5IV5_A	1–276	21–436	3.1E-28
104	1,309	Baseplate Wedge 3 (BW3), baseplate trifurcation unit and tail fiber attachment	Gp7	PF09684	30–169	6–136	6.4E-4

Table 2 (continued)

Gene name	Length of gene product, a.a.	Function (acronym), additional functional details	T4 or other phage ortholog	PDB (with chain ID) and/or PFAM code of best match	Residue range of A511 protein	Residue range of best match	E-value
105	173	Baseplate Wedge 3 Tail Fiber Network (BW3TFN) component	Gp8	5IV5_E	2–173	10–334	1.1E-8
106	1,151	Receptor-Binding Protein (RBP) or Tail Fiber (TF), previously called VrlC	Phage 1358 RBP	4L99	41–110	11–92	78.0
				PF16075 (DUF4815)	9–613	1–580	1.3E-128
107	73	Tail Fiber Assembly chaperone (TFA), putative	Prefoldin beta subunit	2ZQM	1–66	49–110	0.21
108	430	Receptor-Binding Protein (RBP) or Tail Fiber (TF)	Phage phi11 orf56	5EFV	38–283	438–644	8.5E-14
			Zebrafish Caprin-2 C1q domain	4OUS	284–425	6–137	1.3E-12
109	136	Tail Fiber Assembly chaperone (TFA), putative	PBSX protein XkdW	2HG7	16–131	6–101	0.0026

Fig 2E) considering that the corresponding proteins display about 20% sequence identity at best. Notably, no adjustment was made to the position of individual components of the T4 baseplate-derived model that comprises 49 different polypeptide chains belonging to 8 different proteins in multiple copies and yet the T4 baseplate matched the A511 cryoEM density with a precision of individual α-helices or α-helical bundles as described below.

The main component of the conserved core part of the T4 baseplate is the $(gp6)_2$-gp7 heterotrimer, which consists of an α-helical core bundle and a trifurcation unit. These heterotrimers interact with each other via the C-terminal domains of two BW2 gp6 proteins that extend from the trifurcation unit in the opposite tangential directions and form dimers. The third (radial) extension of the trifurcation unit is formed by the BW3 gp7 protein and connects the unit to the tail fiber network. The BW1 gp25 protein is located at the tip of the core bundle and comprises an integral part of the sheath. All these proteins and domains have counterparts in the A511 cryoEM density—there are densities corresponding to the α-helical core bundle, to the trifurcation unit, to the dimeric domains connecting the neighboring trifurcation units, and to the BW1 baseplate-sheath connecting protein (Fig 2A, D, E and F). These features are therefore conserved in the A511 baseplate: The A511 BW1 protein gp102 links the baseplate with the sheath (Fig 2A and D); the BW2 and BW3 proteins gp103 and gp104 form the $(gp103)_2$-gp104 trifurcation unit (Fig 2E); the neighboring units are connected to each other via dimerization of the C-terminal domain of the BW2 gp103 protein (Fig 2F); and finally, the BW3 gp104 protein is responsible for attachment of the tail fiber network (Fig 2A and F).

The central spike complexes of A511 and T4 have similar overall architecture despite targeting different cell envelopes

Bioinformatic analysis shows that the tail tube-spike complex of A511 is formed by the gp94 tube protein (T4 gp19 ortholog), gp100 baseplate hub 1 (BH1, T4 gp48 ortholog), gp98 baseplate hub 2 (BS2, T4 gp27 ortholog), and gp99 baseplate spike (BS, T4 gp5 ortholog) (Table 2). In addition to these proteins, the T4 tail tube-spike complex contains gp54 (which forms the first disk of the tube and whose structure is identical to that of the main tail tube protein gp19) and the baseplate spike tip (BST) protein gp5.4. The complete structure of the T4 tail tube-spike complex (gp19-gp54-gp48-gp27-gp5-gp5.4) accounts for most of the A511 tube-spike complex cryoEM density with certain differences in the region of the BH2-BS complex (Fig 2A–C). The cryoEM density shows that the A511 central spike BH2-BS complex (gp98–gp99) is more massive and has a larger diameter than its T4 ortholog (Fig 2A). The BH2 gp98 protein is twice as long as T4 BH2 gp27 (795 vs. 391 residues) and contains a large mostly α-helical domain whose function is unknown (residues 340–520) and an additional C-terminal domain (residues 624–794) with a predicted peptidoglycan hydrolase function. The cryoEM density shows two additional domains (per BH2 gp98 monomer) connected to the T4 BH2 gp27-like hub structure. The crystal structure of the peptidoglycan endopeptidase RipA of *Mycobacterium tuberculosis* (PDB code 4Q4G) (Squeglia *et al*, 2014; Fig 2A), which is predicted by HHpred to have a similar fold (Table 2; Soding *et al*, 2005; Alva *et al*, 2016), can be fitted into one of these extra densities. This domain is likely to lacerate the host murein layer during infection. Notably, the enzymatic activity
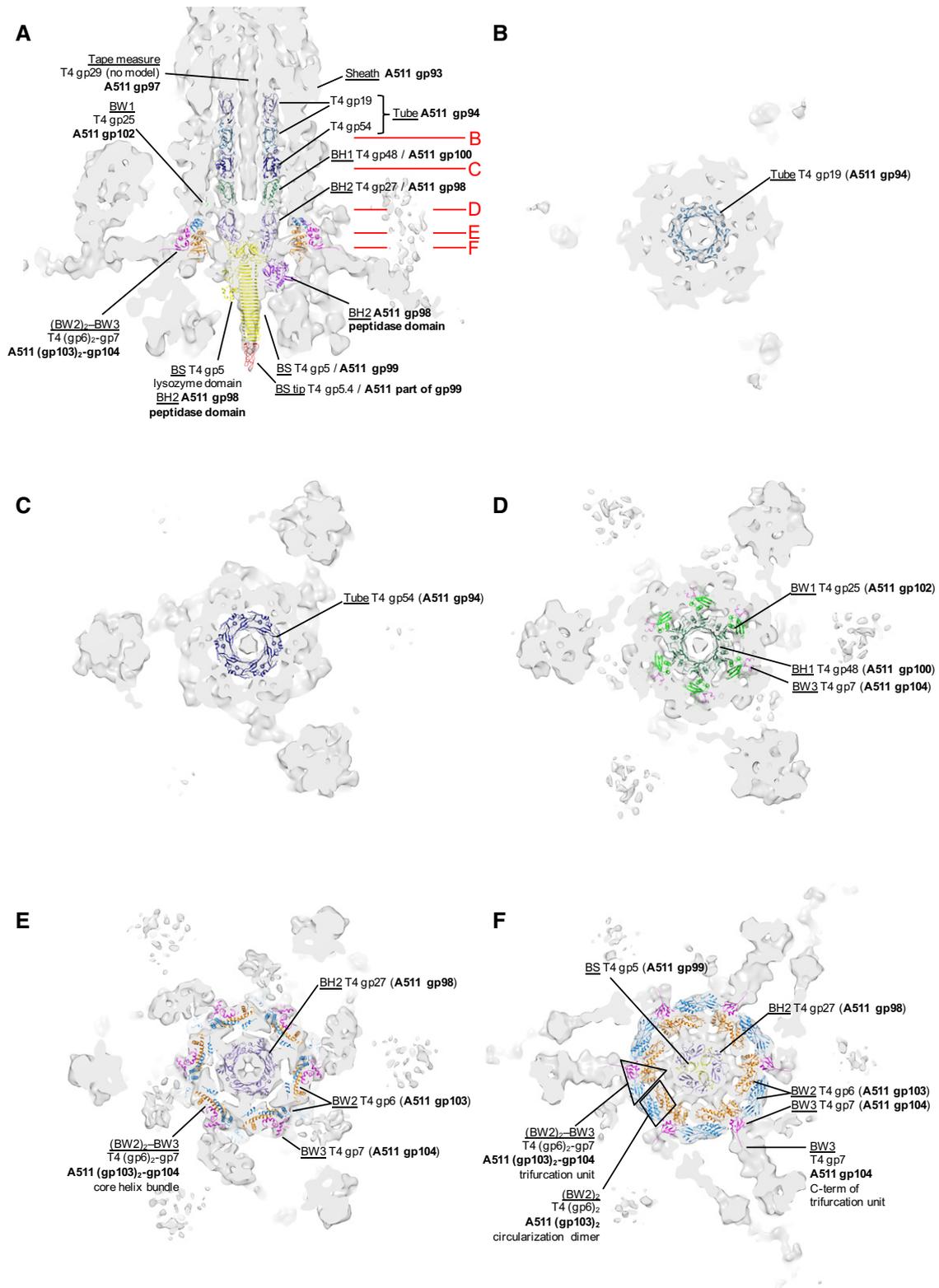
Figure 2. Fitting of the pre-attachment T4 tail tube-baseplate core complex into the A511 extended tail cryoEM map.

A–F   Atomic structures of T4 proteins are shown as ribbon diagrams of various colors and labeled with T4 and A511 gene product names as well as with their functional orthologs common to all contractile-like systems (e.g., BH1, see Table 2). The putative endopeptidase domain of A511 gp98 is modeled by the crystal structure of RipA of *Mycobacterium tuberculosis* (colored purple). Red lines and labels in panel (A) indicate the position of end-on views shown in panels (B through F) (looking from the capsid).

Table 3. Local correlation coefficients—as defined and calculated by the UCSF Chimera program (Pettersen *et al*, 2004)—characterizing the fit of crystal structures into cryoEM maps.

UCSF Chimera was used to render the crystal structures as density maps by describing each atom as a Gaussian distribution with a width proportional to map resolution (see Table 1) and amplitude proportional to the atomic number. The values in parentheses are correlation coefficients that take into account only the strong features of the maps derived from atoms.

Protein	Fit into the extended map	Fit into the contracted map
BW3TFN gp105 dimer 1 (baseplate proximal)	0.62 (0.94)	0.59 (0.89)
BW3TFN gp105 dimer 2 (middle)	0.62 (0.94)	0.58 (0.90)
BW3TFN gp105 dimer 3 (baseplate distal)	0.64 (0.93)	0.53 (0.87)
Three gp105 dimers from the extended map fitted into the contracted map as a unit		0.63 (0.88)
Tube-spike complex	0.59 (0.89)	
Conserved part of the wedge (six wedges as a unit)	0.56 (0.86)	0.44 (0.69)
Tube-spike-wedges as a unit	0.62 (0.88)	
Phi11 RBP residues 437–537 (N-terminal bulge of RBP gp108)	0.77 (0.96)	
Phi11 RBP residues 550–635 (C-terminal bulge of RBP gp108)	0.67 (0.95)	
C1q trimer (C-terminal domain of RBP gp108)	0.53 (0.90)	

associated with the central spike complex and targeting the cell wall is conserved in both T4 and A511.

The function of the central spike complex is to create a passage through the cell envelope of the target bacterium to allow the tail tube to reach the plasma membrane during sheath contraction. T4 and A511 infect hosts with markedly different cell envelope organizations (Gram-negative *E. coli* and Gram-positive *Listeria*, respectively), so the similarities in the overall organization of their central spike complexes are rather remarkable. Not only are the lengths of the two nearly identical [the lack of the spike tip protein in A511 is compensated by a longer C-terminal domain of the gp99 spike (Fig 2A)], but the location of the peptidoglycan hydrolase domain in the complex is the same. While no enzymatic domain is predicted in the BS gp99 spike of A511, the site of the T4 BS spike protein gp5 lysozyme domain (Kanamaru *et al*, 2002) is occupied by the putative peptidase domain of A511 BH2 gp98 hub protein giving the BS-BH2 spike complexes of T4 and A511 nearly identical shape (Fig 2A). The high degree of structural conservation of T4 and A511 central spike complexes and the fact that *Listeria* does not contain an outer membrane suggest that the central spike or at least some part of it in phages of Gram-negative bacteria is translocated into the cytoplasm of the host cell. This is consistent with the function of the related T6SS organelle that is known to translocate the spike complex directly into the cytoplasm of bacterial cells (Vettiger & Basler, 2016). At the same time, the envelope-attacking part of the A511 BS gp99 spike (residues 328–510) is predicted to form a coiled coil structure whereas this domain is a triple-stranded β-helix in T4 gp5 (Browning *et al*, 2012), which is further capped by the gp5.4 BST protein. The coiled coil domain is conserved in BS spike proteins of all A511-like phages suggesting a functional requirement for the interaction with the cell envelope of Gram-positive bacteria.

The A511 baseplate-tail fiber complex has threefold symmetry in the pre-host attachment state

The baseplate and the tail fiber network structure of A511 are dominated by twelve large pyramid-shaped densities that are situated around the periphery of the baseplate above and below its plane (Fig 3). The pyramids display clear threefold symmetry that makes it possible to segment them out into separate entities. The pyramids are attached with their apexes to six fibers (two pyramids per fiber) in opposite orientations—with a base pointing roughly toward and away from the phage head (Figs 1A, D and G, and 3). The fibers form rays of a star-like structure: each fiber starts at the baseplate, extends ~260 Å away from it, makes a 157° turn, and returns to the baseplate (Fig 1G). Adjacent rays are not co-planar, and the planes that run through them form angles of 82° and 60° relative to the tail's axis, resulting in overall threefold symmetry (Fig 1D). The alternate fibers start and end at the same place at the periphery of the conserved core part of the baseplate. The structures of all the pyramids are very similar, although the distal pyramid of the 60° fiber is very disordered because it interacts with the rest of the structure at a single point—at its apex (Fig 3A). The threefold symmetry of the pyramids suggests that they are formed by trimeric proteins, a typical feature of phage fibers and tailspikes that are situated around the periphery of the baseplate and function to specifically recognize binding partners on the surface of a target cell (Williams *et al*, 2008; Buth *et al*, 2018).

The proximal part of the tail fiber contains three gp105 dimers

Guided by bioinformatic analysis (Table 2), we cloned and expressed in *E. coli* (in various combinations and as domain deletion variants) genes 104–109, which were predicted to comprise the tail fiber subcluster of A511 in our earlier study (Habann *et al*, 2014). The only protein that could be purified in amounts sufficient for crystallization was T4 gp8 ortholog gp105. The crystal structure of gp105 was then determined with the help of the single anomalous diffraction technique (Rice *et al*, 2000) followed by non-crystallographic symmetry averaging (Rossmann & Blow, 1962). Gp105 formed a gp8-like dimer (Leiman *et al*, 2003) in which the central part has been retained but the peripheral parts have been removed (Fig 4A–F). As the molecular weight (MW) of gp105 is almost exactly half of that of gp8 (19.1 kDa vs. 38.0 kDa per monomer), gp105 could be considered as a "lean" version of T4 gp8. The monomers of gp105 and gp8 can be superimposed with a root-mean-square deviation of 2.6 Å between 155 C_α atoms in the alignment (89% of gp105 residues) with a sequence identity of only 18% (Fig 4G and H).
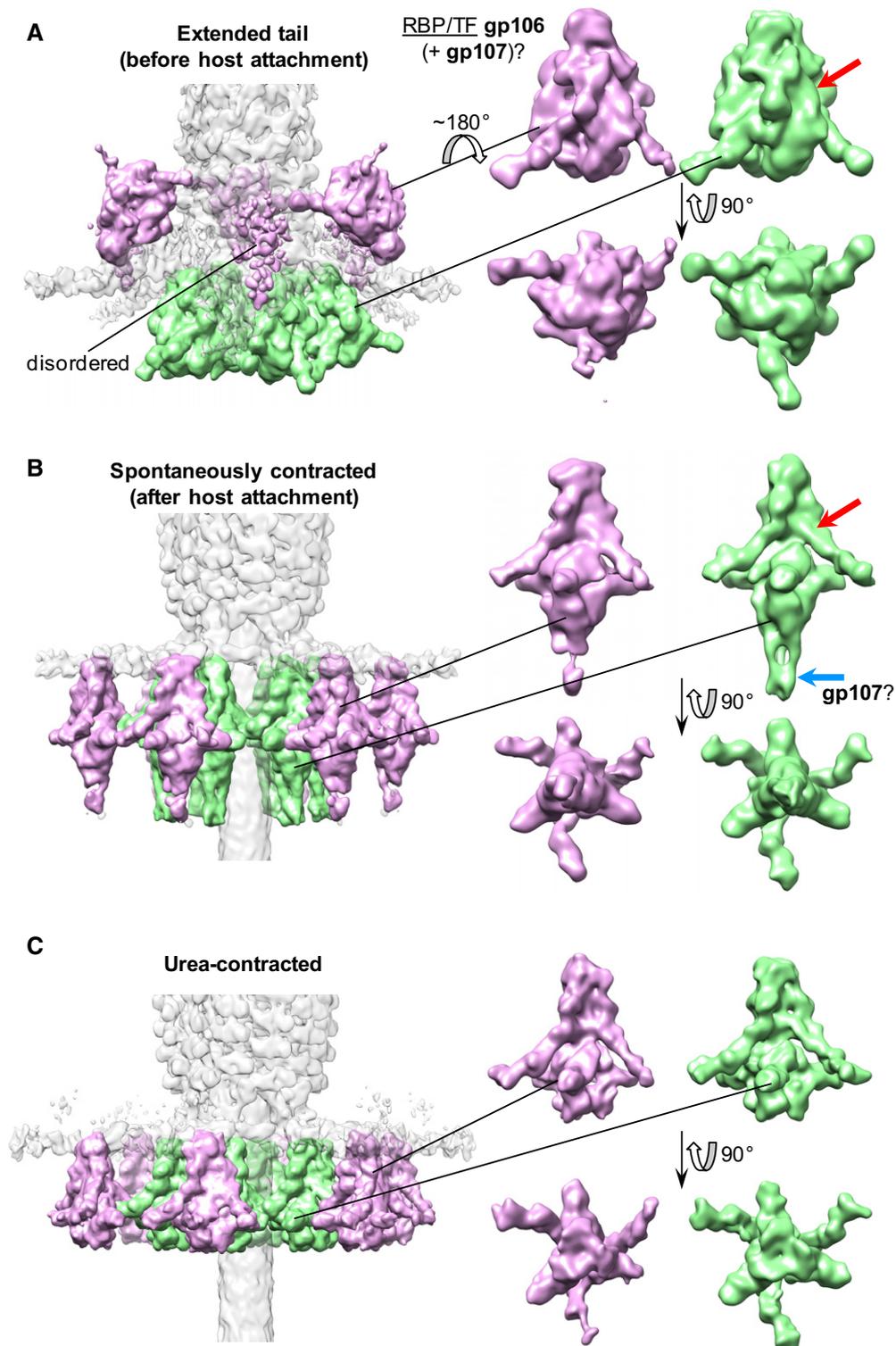
Figure 3. The A511 baseplate carries twelve very large pyramidal densities that display threefold symmetry.

The pyramids correspond to gp106 and, possibly, gp107 proteins.

A   Structure of the A511 baseplate in the pre-host attachment state (extended sheath). The pyramids above and below the plane of the baseplate (colored plum and light green, respectively) are very similar (this color scheme is maintained in all panels). Three pyramids that do not interact with the sheath are disordered. The red arrow points to a density feature that is clearly different in the post-attachment conformation of the pyramid.

B, C   Structure of the spontaneously- and urea-contracted A511 tail (respectively) with the baseplate in the post-host attachment state. The blue arrow points to a density feature that is missing in the urea-contracted structure.

We then used the programs COLORES (Wriggers & Chacon, 2001; Wriggers, 2010) and UCSF Chimera (Pettersen *et al*, 2004) to determine the positions of gp105 dimers in the pre-attachment cryoEM map of the A511 baseplate (Fig EV2, Table 3). COLORES placed two gp105 dimers next to each other in the fiber that emanates from the gp104 trifurcation domain (Fig 5A). By visual inspection of the map an additional copy of gp105 dimer was identified immediately after the first two dimers, further along the fiber.
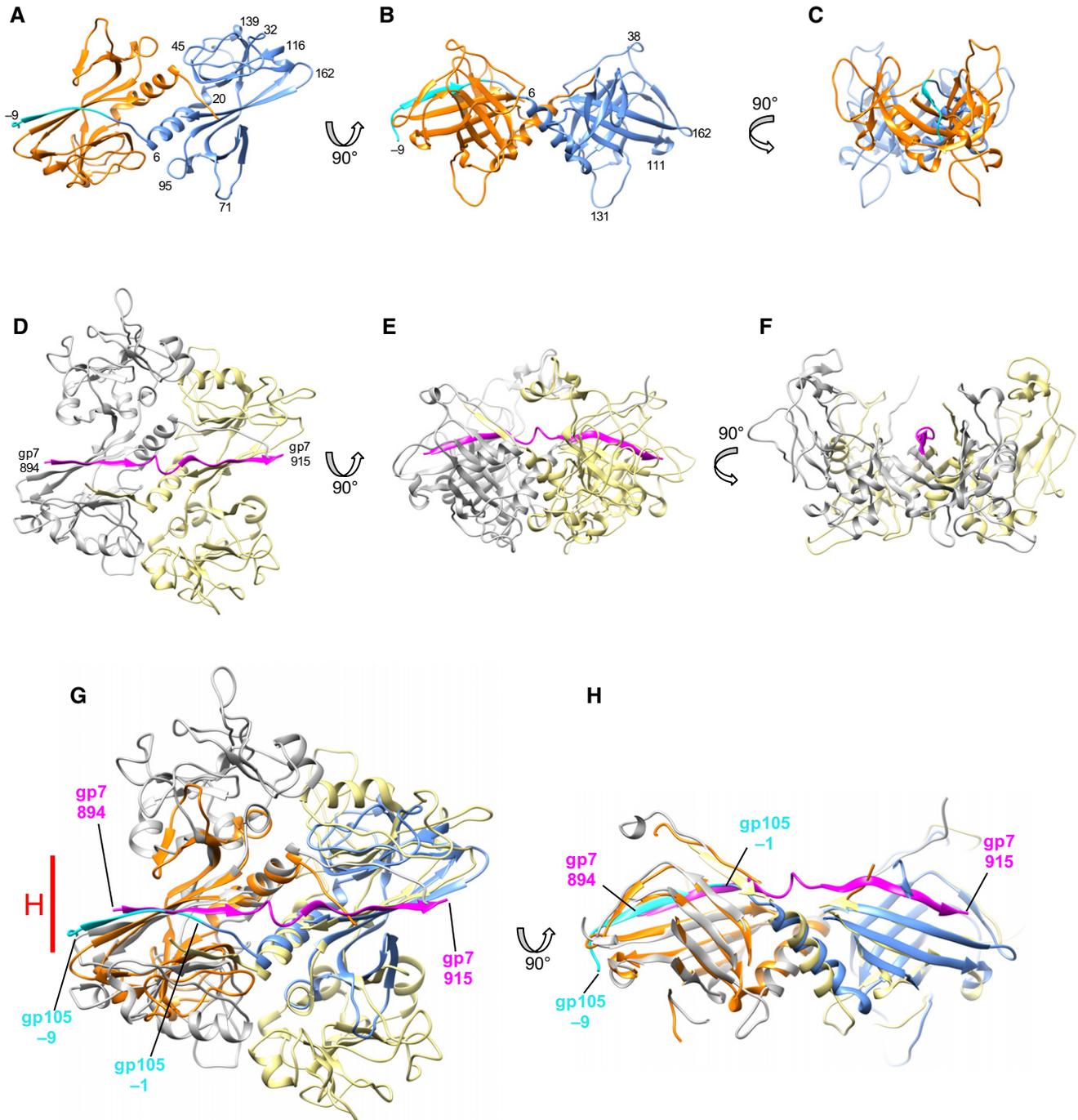

Figure 4. Crystal structure of gp105 and its comparison with T4 gp8.

A–C   Three orthogonal views of gp105 dimer. The uncleaved N-terminal tag is in cyan. Residue numbers are given in strategic positions.

D–F   Three orthogonal views of T4 gp8 dimer extracted from the T4 baseplate structure in the same orientations as gp105 in panels (A–C). The fragment of T4 gp7 that spans the gp8 dimer is in magenta.

G   Superposition of T4 gp8 and gp105 dimers. The color scheme is as in panels (A–F). The red line indicates the region shown in panel (H).

H   Gp7 (magenta) nearly perfectly matches the gp105 N-terminal tag (cyan) upon the superposition of T4 gp8 and gp105 dimers.

Figure 5. The structure and conformation of the A511 tail fibers/receptor-binding proteins.

A–C Panels (A and C): the pre-host attachment state. Panel (B): the post-attachment state. The atomic structure of the conserved tube-baseplate core complex (derived from the T4 tube-baseplate complex) in the pre- and post-attachment states is fitted into the cryoEM maps. The color scheme is the same as in Fig 2. BW3 gp104 and its ortholog T4 gp7 are colored magenta. The putative chain of gp104 crossing three gp105 dimers is shown as a thick coil. (C) A thin slice through the pre-attachment state cryoEM map is shown. The plane of the baseplate is about 8° out of the plane of the paper. The distal part of the A511 tail fiber is formed by the gp108 trimer, whose structure is modeled with homologous domains that are fitted into the pre-attachment baseplate cryoEM map. The structures are shown as ribbon diagrams and colored in a rainbow pattern with N terminus in blue and C terminus in red. The numbers indicate the N- and C-terminal residues of the gp108 sequence that match the start and end of the homologous structures. The smaller insets show cross sections of the fiber cryoEM density with fitted crystal structures of domains homologous to gp108.

The position of the third gp105 dimer was refined with the help of COLORES restricting the search limits to this particular location (Fig 5A). Thus, three gp105 dimers comprise a large fraction of the proximal part of the A511 tail fiber, which was previously called "long tail fiber" and whose protein composition was unknown (Habann *et al*, 2014).

Interestingly, the interaction of gp105 dimers in the crystal mimics their interaction in the phage fiber (Fig EV2). Three gp105 dimers related by symmetry of a 3_2 crystal axis of the P3$_2$21 crystal lattice nearly perfectly match the structure of the three gp105 that were fitted into the cryoEM density of the fiber. The N-terminal hexa-histidine tag that was introduced for the purpose of affinity purification, and that extends the central β-sheet as described above, also participates in the crystal lattice contacts that are responsible for the association of gp105 dimers into a fiber (Fig EV2).

T4 gene *8* and A511 gene *105* are located immediately downstream from the T4 BW3 gene *7* and A511 BW3 gene *104*, respectively (Table 2). Gp8 and gp105 are homologous (Fig 4G and H) and are either involved in tail fiber attachment or form the integral part of the fiber network. We, therefore, propose to call gp105 and its orthologs BW3-tail fiber network proteins or BW3TFNs. Such proteins are found in many contractile tail bacteriophages (Fig EV3). In some instances, a *BW3* gene can contain a module encoding the BW3TFN function (Fig EV3).

BW3 gp104 is also a component of the proximal part of the tail fiber

The BW3TFN gp8 dimer is next to the trifurcation domain of the BW3 gp7 protein in the T4 baseplate, a location that is very similar to that of the baseplate-proximal BW3TFN gp105 dimer in the A511 baseplate (Fig 5A). The polypeptide chain of gp7 runs across the surface of the gp8 dimer end to end. Gp7 extends the central β-sheet of the gp8 dimer by the β-sheet augmentation mechanism, which is also employed in the organization of the contractile sheath (Ge *et al*, 2015; Kudryashev *et al*, 2015) (Fig 4D–F). Both the central β-sheet and the trough that can accommodate an extended polypeptide chain are conserved in A511 BW3TFN gp105 (Fig 4G and H). In the crystal structure of gp105, the trough is occupied by the uncleaved N-terminal tag, which extends the central beta-sheet in a manner identical to that of T4 BW3 gp7 protein. Thus, A511 BW3TFN gp105 retains the structure and functionality of T4 BW3TFN gp8 and is likely to bind the chain of A511 BW3 gp104 protein in a similar extended conformation.

Building up on this hypothesis, we modeled the structure of BW3 gp104 as it crosses the surface of three BW3TFN gp105 dimers by extracting the coordinates of gp7 from the superposition of

(gp8)$_2$-gp7 complex onto the respective gp105 dimer (Fig EV4). The three putative gp104 fragments form a nearly continuous chain that starts at the C terminus of the BW3 gp104 trifurcation unit domain and extends to the elbow turn region of the fiber where it forms a large disordered domain (Fig 5A). At least two additional "Bulge" domains stick out from the gp104-gp105 fiber. One is near the trifurcation unit, and the other is near the middle BW3TFN gp105 dimer. Both are likely to be formed by gp104 and both participate in binding of the large pyramidal proteins to the fiber.

Gp106 forms the pyramidal densities attached to the proximal part of the tail fiber

The MW and the identity of the proteins comprising the large pyramidal densities can be estimated with the help of the gp105 crystal structure. The MWs of the upward- and downward-base pointing pyramids are about 326 kDa and 388 kDa, respectively, or 109 kDa and 129 kDa per monomer taking into the account their threefold symmetry. The volume of the pyramid is sufficient to accommodate a trimer of gp106 (128 kDa), whose presence in the baseplate was established previously (Habann *et al*, 2014). As there are 12 trimers or 36 copies of gp106 per particle, this protein should be easily detectable on a Coomassie-stained sodium dodecyl sulfate–polyacrylamide electrophoresis (SDS–PAGE) gel of the A511 particle, which is indeed the case—the corresponding band is a major component of the virion (Fig EV1B).

The distal part of the tail fiber is formed by gp108 trimer

Bioinformatics and the analysis of cryoEM map suggest that the distal part of the A511 cryoEM fiber is formed by the trimer of gp108 protein that was previously shown to specifically bind to *Listeria* cells (Habann *et al*, 2014). In the cryoEM reconstruction of the A511 tail presented here, this part of the fiber is folded back and interacts with the baseplate (Fig 1A, D and G). The C-terminal domain of gp108 (residues 284–430) is predicted to form a C1q-like domain (Table 2) (Miao *et al*, 2014). This jelly roll-like domain is found in a number of eukaryotic signaling and immune system proteins where it forms a compact trimer. The trimeric C1q domain can be fitted into the globular density at the distal end of the fiber, which contacts the baseplate (Fig 5C, Table 3). The N-terminal half of gp108 (residues 38–283) contains two domains that are homologous to the tandem C-terminal domains of the receptor-binding protein of *Staphylococcus* phage phi11 (Koc *et al*, 2016; Table 2). When fitted into the A511 fiber cryoEM density, these domains are about 60 Å away from each other, which is in good agreement with the length of the spacer (50 residues) separating them in the gp108
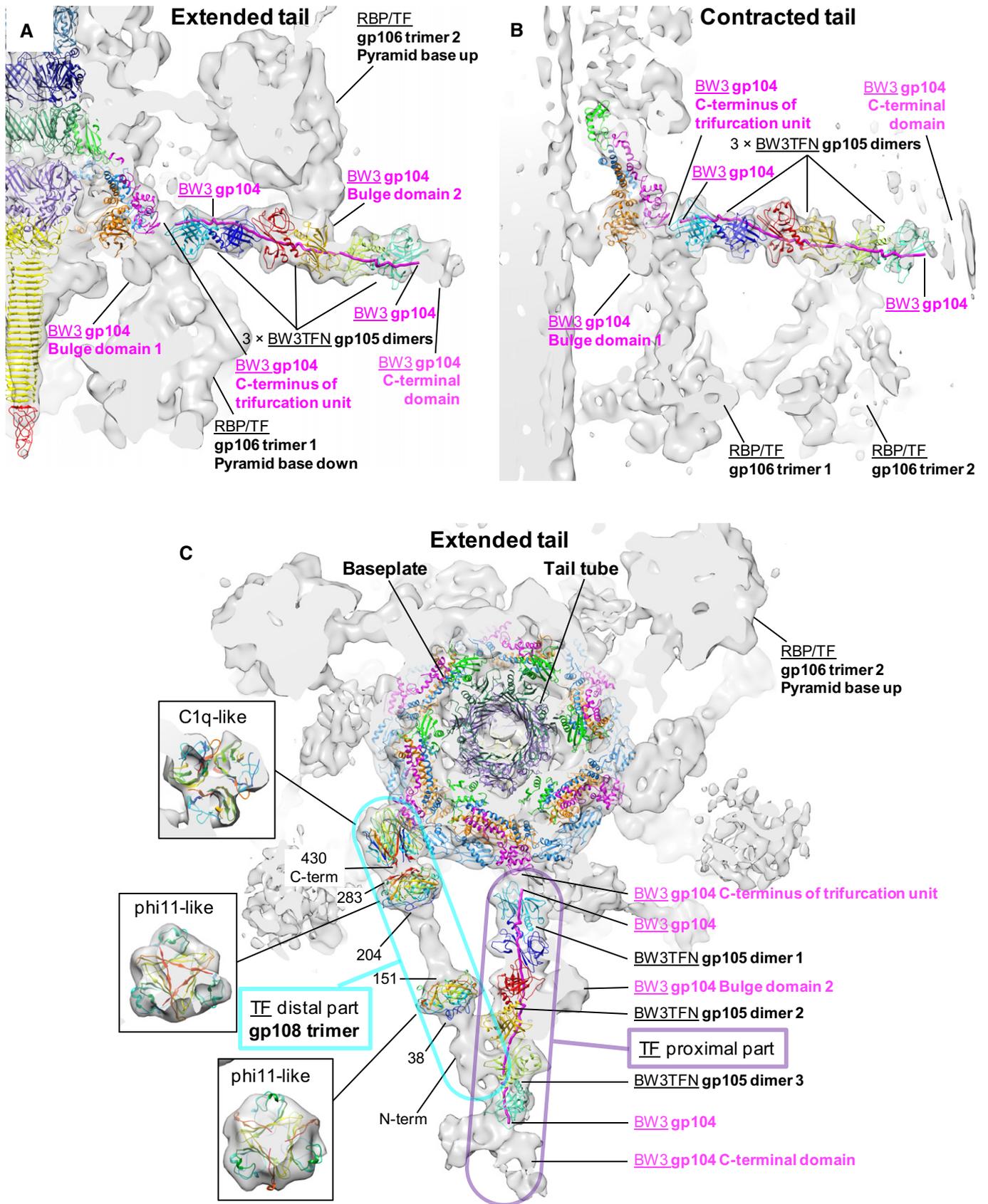
Figure 5.

amino acid sequence (Fig 5C, Table 3). Notably, a similar tandem domain is found in the central part of the R-type pyocin receptor-binding fiber where it was proposed to interact with the host cell surface (Buth *et al*, 2018).

It is now possible to explain the organization of A511 fibers (Fig 5C). The fiber starts at the BW3 gp104 trifurcation domain. Its proximal part is formed by three BW3TFN gp105 dimers that interact with each other and BW3 gp104, which runs across the surface of gp105 dimers and forms two Bulge domains that stick out sideways from the gp104-gp105 complex and bind the gp106 pyramids. The "Elbow" domain is formed, most likely, by the C-terminal part of BW3 gp104. The fiber than makes a sharp turn and the rest of its structure is formed by trimeric RBP gp108. The N-terminal domain of RBP gp108 is attached to BW3 gp104, whereas its C-terminal domain interacts with the baseplate.

Upon host attachment, all 12 copies of RBP/TF gp106 pyramids point toward the host cell surface and the baseplate-tail fiber complex becomes sixfold symmetric

We first attempted to produce a uniformly contracted specimen by adding 2 M urea to the A511 sample (Leiman *et al*, 2004; Fokine *et al*, 2013), but this treatment caused complete disintegration of the phage. A 1-h dialysis into a buffer containing 2 M urea resulted in a homogeneously contracted specimen, but even in this case, and unlike T4, the A511 virion experienced some protein loss as evidenced by the structure of gp106 pyramids in the absence and in the presence of urea (Figs 1 and 3B and C). Furthermore, most particles contracted by urea had empty capsids and their tube channels were also empty (Fig 1F and I) suggesting that urea destabilizes the membrane-interacting tip of the tail tube and "uncorks" the particle.

The structure of the baseplate associated with the contracted sheath (the post-host cell attachment conformation) is sixfold symmetric and all the gp106 proteins now point toward the potential host cell surface (Figs 1 and 3). Besides the rigid body rotation, the gp106 proteins undergo a significant structural transformation. The sides of the gp106 pyramid are now concave, and the spontaneously contracted sample displays a large protrusion below the pyramid's base. A similar structural transformation was reported earlier for the phage phi812 gp122-gp123 "tripod complex", a A511 gp106 ortholog (Novacek *et al*, 2016). SDS–PAGE of the non-contracted and urea-treated particles did not reveal a detectable shift in the mass of the gp106 protein (Fig EV1B), suggesting that proteolysis is either taking place before tail contraction and urea treatment or the lost density corresponds to a separate protein. In the latter case, gp107 is a strong candidate to account for the missing density because gp106 and gp107 are likely to interact (their orthologs are very well conserved even in defunct clusters of *Dichelobacter nodosus* and its relatives (see Appendix). Even though no orthologs of gp107 have been found in the proteomes of A511-like phages so far (Habann *et al*, 2014), they constitute a very small fraction of the virion material (MW of gp107 is 8.6 kDa) and are very difficult to detect on SDS–PAGE.

A511 TF/RBP proteins display features common to TF/RBPs of T4 and p2 phages

Reorientation of the peripheral RBP/TF gp106 pyramids upon host cell binding is very reminiscent of the structural transformation of the baseplate of lactococcal phage p2 (Fig 3). The p2 baseplate is equipped with six trimeric receptor-binding proteins that point their "bases" roughly toward the phage head in the pre-host attachment state and point away from the phage head, toward the host cell surface in the post-host cell attachment state (Sciara *et al*, 2010).

At the same time, the conformation of the A511 distal part of the tail fiber in the pre-host attachment baseplate structure (Figs 1A, D, G and 5C) is remarkably similar to that of the T4 short tail fiber gp12 RBP, which is also folded back so that its C-terminal domain interacts with the baseplate. In both phages, the fiber remains in this stowed conformation until the phage finds its host cell (Kostyuchenko *et al*, 2003).

Yet another feature of A511 gp108 that is common to other TFs is the presence of a small putative assembly chaperone protein gp109, which is encoded by a gene immediately downstream from the TF gene (Table 2). A typical representative of a TF-chaperone pair is the PA0620-PA0621 proteins of R-type pyocins (Buth *et al*, 2018). Interestingly, the PA0620 TF also contains a pair of phi11-like domains roughly in the middle. The chaperone gene of T4 gp12 TF is, however, not immediately downstream from it (gene *57A*) (Dickson, 1973; van Raaij *et al*, 2001).

Transformation of the A511 baseplate structure upon host cell binding is similar to that of T4

Structural changes of the A511 baseplate upon sheath contraction match those of the T4 baseplate. The distal part of the tail fibers and RBPs undergo a massive transformation whereas the structural change of the actual baseplate (gp102-(gp103)$_2$-gp104 or BW1-(BW2)$_2$-BW3 complex) and the proximal part of the tail fibers (three BW3TFN gp105 dimers) is much more subtle. The T4-derived conserved baseplate core in the contracted state (the same composition as for the extended tail baseplate barring the central hub-spike proteins) fits the A511 cryoEM map—as a rigid unit with no individual adjustment—very well (Fig 6A–E, Table 3). The interpretation of the A511 contracted tail cryoEM map is consistent with that in the extended state. The C-terminal dimerization domain of the T4 BW2 gp6 protein matches a twofold symmetric density, which likely corresponds to the C-terminal domain of the A511 BW2 gp103 protein (Fig 6D). The (gp6)$_2$-gp7 α-helical core bundle and the trifurcation unit fit a trimeric feature of the A511 cryoEM density, which likely corresponds to the A511 (gp103)$_2$-gp104 heterotrimer (Fig 6A, B, D and E). The conservation of structure and structural transformation of the baseplate in such distantly related phages as T4 and A511 suggests that other contractile tail-like systems undergo a similar conformational change.

The distal part of the A511 tail fiber, formed by gp108, is disordered in both contracted tail samples. Surprisingly, the structure of the proximal part of the fiber in the post-attachment state is virtually identical to that in the pre-attachment state. Three gp105 dimers from the pre-attachment state fit the post-attachment density as a large rigid body perfectly with a very small rotation (compare Fig 5A and B and see also Table 3). Despite the nearly 180° rotation of the RBP/TF gp106 pyramid-shaped proteins, the fiber to which they are attached remains in place and changes little, as if gp106 is a gymnast swinging on a high bar. How this is accomplished remains to be determined.
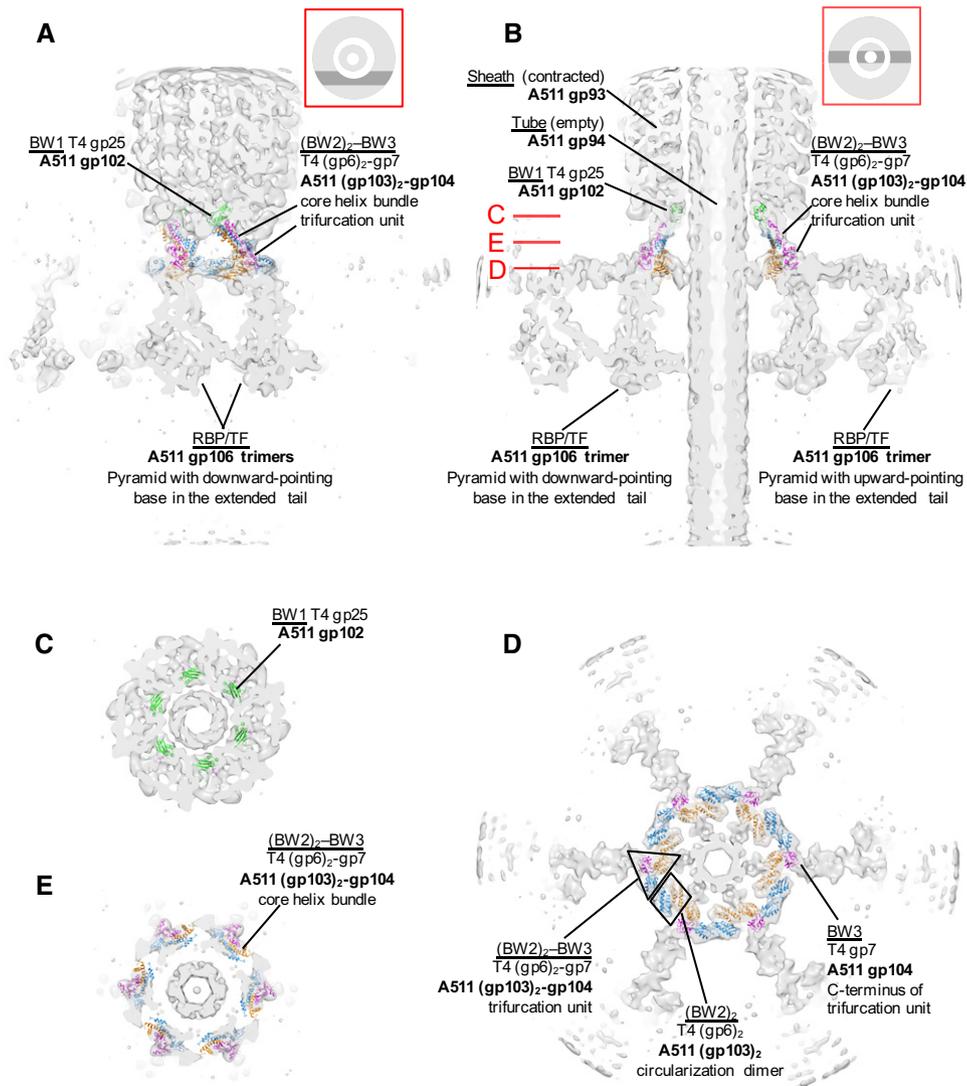
Figure 6. Fitting of the conserved part of the T4 baseplate in the post-host attachment state into the A511 urea-contracted tail.

A, B   Cut-away views through the structure at positions indicated in the inset schematic end-on views. The T4 proteins are shown in the ribbon diagram representation with the same color scheme as in Fig 2.

C–E   Cut-away end-on views (looking from the capsid) at positions indicated with the red lines in panel (B).

Interaction of A511 with the *Listeria* cell wall involves a partially contracted intermediate and can be divided into several defined stages

To investigate the function of the baseplate and fibers in host cell attachment, we analyzed the structure of A511 in the presence of *Listeria* cell wall by cryoET (Fig EV5, Movie EV1). We found that contraction of the sheath is accompanied by binding of the RBP/TF gp106 pyramids to the *Listeria* cell wall. This interaction is likely mediated by the domain (or separate protein, e.g., gp107) that protrudes from the base of the gp106 pyramid (Fig 3) and which is lost in the urea-contracted sample because no interaction between the urea-contracted phage and the cell wall was observed upon co-incubation.

CryoET data showed that a large fraction of particles featured a partially contracted tail (Fig EV5). In tomographic slices of partially contracted particles, the tail tube is not visible in the extended part of the tail, but it can be clearly seen in the contracted segment where the sheath separates from the tube (Fig EV5, Movie EV1). To determine whether the partially contracted structure is an intermediate of the contraction process or a defective particle arrested in this conformation, we collected cryoET data at 5, 20, and 80 min after the cell wall was added to the virus sample. The fraction of extended and partially contracted sheaths decreased over time whereas that of the fully contracted increased (Fig 7A) indicating that partially contracted particles were indeed in an intermediate state. Close to 90% of particles were fully contracted after 80 min of incubation with only about 10% still extended or partially
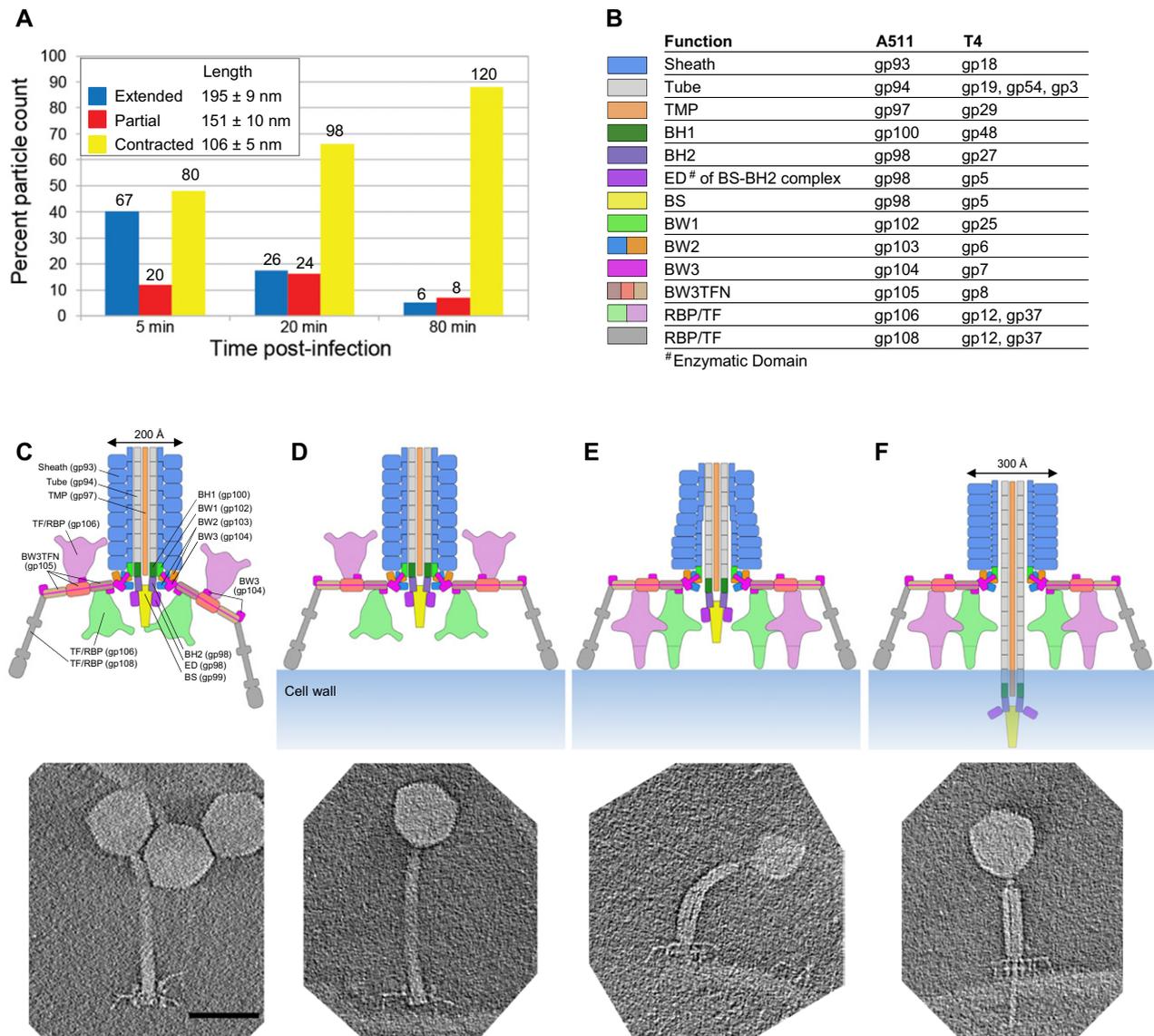
Figure 7. Structural transformation of A511 tail upon binding to *Listeria* cell.

A   Percentage of phage particles in the extended, intermediate, and contracted states after 5, 20, and 80 min of incubation with *L. monocytogenes* cell walls. The numbers above the bars show the number of particles contained in the tomograms. The average length of the tail and the standard deviation for each of the three states are given next to the color legend.

B   The color code for proteins that were located in A511 cryoEM maps (upper panels C, D, E, F) and their T4 orthologs. The functions are identified with acronyms that are given in Table 2.

C   Structure of the A511 tail in the pre-attachment state. Here and elsewhere in this figure, the EM image in the lower panel is a slice through the cryoET reconstruction. Note that in the presence of the *Listeria* cell wall the gp108 fibers are no longer in their stowed conformation but instead are fully or partially unraveled.

D   Gp108 fibers attach to the host cell wall but the sheath is not yet contracted.

E   RBP/TF gp106 pyramids reorient to point their bases toward the cell surface, change their conformation, and bind to the cell wall. A part of the cell wall-interacting domain is possibly formed by gp107. The baseplate-proximal part of the sheath is in a contracted state, whereas the capsid-proximal part is still in an extended state. The baseplate-proximal part of the sheath contains a segment where the tail tube is clearly visible because it no longer interacts with the sheath (lower panel).

F   The post-attachment state. The tail is fully contracted, and the tail tube has pierced through the cell wall. The capsid appears full indicating that DNA injection has not yet begun.

Data information: Scale bar for lower panels (C, D, E, F): 100 nm.

contracted. The partially contracted particles had a fairly uniform tail length (Fig 7A), which corresponded to about 50 ± 10% of the sheath being fully contracted (neglecting the transition region).

Combining all the available data makes it possible to create a time-lapse sequence of the A511 infection process (Fig 7B–F, Movie EV2). The "single particle" cryoEM reconstruction of A511

pre-attachment baseplate described earlier with the distal part of the tail fibers neatly tucked around the baseplate is a most populous state of the particle when it is far away from the host cell (Figs 1 and 5C). One of the most common conformations of the phage in the sample containing the *Listeria* cell wall, but not bound to it, is a particle with three unfolded fibers (Fig 7C). Binding of the distal part of the tail fiber to the *Listeria* cell wall constitutes the initial interaction of the phage with the host and strongly supports our assignment of this density as RBP/TF gp108, which is known to bind to *Listeria* cells (Habann *et al*, 2014). This interaction results in no discernable changes to the particle structure (Fig 7D). This initial binding is followed by a conformational change and reorientation of gp106 pyramids and transformation of the baseplate into the post-attachment state (although the sequence of these two events cannot be determined here; Fig 7E). The sheath starts to contract, but only the baseplate-proximal part of it is clearly contracted. The head-proximal part of the sheath appears to be still in the extended state. In the final state, all gp106 pyramids and gp108 fibers point toward the cell wall and interact with it (Fig 7F). The baseplate takes its double-layer appearance that is common to Spounavirinae phages (Klumpp *et al*, 2010). Similar to T4 (Leiman *et al*, 2004), sheath contraction and DNA injection are not linked in A511, as demonstrated by the prevalence of phages with contracted tails and full capsids (Fig EV5).

The tail contraction signal propagates from the baseplate through the sheath as a domino wave

We would like to conclude that we show here—for the first time in near-native conditions—that the contraction propagates through the sheath in a wave-like motion starting at the baseplate. This is a direct confirmation of a hypothesis that was put forward more than 50 years ago in studies that involved triggering the contraction with chemical or physical agents and/or sample fixation using chemical agents (Eiserling, 1967; Simon & Anderson, 1967a,b; Donelli *et al*, 1972; Benz & Goldberg, 1973; Moody, 1973). Considering the overall structural similarity of A511 baseplate to that of T4 and their similar structural transformation associated with sheath contraction (Schwarzer *et al*, 2012; Kostyuchenko *et al*, 2003, 2005; Leiman *et al*, 2004; Aksyuk *et al*, 2009; Hu *et al*, 2015; Taylor *et al*, 2016), we can extend our findings to all contractile tail-like systems—all contractile tails of phages, R-type pyocins, Photorhabdus Virulence Cassette and other tailocins, and the Type VI Secretion System (Taylor *et al*, 2018). In all these systems, the contraction is likely also triggered by the baseplate and propagates through the sheath in a domino-like fashion.

Materials and Methods

Bacteria strains, growth conditions, and bacteriophage propagation

Listeria ivanovii strain WSLC 3009 (SV 5) was used to propagate phage A511. Cells were grown overnight in half-strength brain–heart infusion medium (½ BHI; Biolife, Milan, Italy) on a shaker incubator at 30°C. Phages were propagated by adapting previously described methods (Loessner & Scherer, 1995). Briefly, 20 ml

of an overnight bacterial culture was added to 1 l of pre-warmed (30°C) ½ BHI. Previously purified phage stocks were also added to a final concentration of 10^5 pfu/ml. This initial culture was incubated to an OD_{600} of about 0.1. At this point, additional phages were added to a final concentration of about 2×10^7 pfu/ml. Incubation continued until culture clearing for approximately 2 h when the solution was placed at 4°C to prevent the growth of resistant bacteria. Bacterial cellular debris was removed by centrifugation at 6,000 g for 15 min at 4°C. Phages were purified by addition of 10% PEG 8.000 (100 g/l of media) and 1 M NaCl. After overnight incubation in ice water, the solution was centrifuged at 10,000 g for 15 min at 4°C. Precipitate was resuspended in SM buffer (50 mM Tris–HCl pH 7.5, 100 mM NaCl, 8 mM $MgSO_4$) and phages purified by CsCl gradient centrifugation at 76,000 g for 18 h at 4°C (Klumpp *et al*, 2008). To elicit phage contraction, purified phages were dialyzed for 2 h against 2 M urea in SM buffer at 4°C (Fokine *et al*, 2013).

Preparation of *Listeria monocytogenes* cell fragments for cryo-electron tomography

To obtain preparations of protein-free cell walls in which only the peptidoglycan and teichoic acids are preserved, cell cultures were processed as previously described (Wendlinger *et al*, 1996). An overnight culture of *L. monocytogenes* cells grown in ½ BHI broth at 30°C on a shaker incubator was inoculated (1/1,000 dilution) in to the same medium and grown at 30°C until the optical density OD_{600} reached 0.8–1.0. Bacteria were harvested by centrifugation at 7,000 g for 10 min, resuspended in SM buffer, and stored at −20°C overnight. Upon thawing, the cells were heated at 100°C for 20 min and then disrupted by three runs through a pressure cell homogenizer (Stansted Fluid Power Ltd., Model SPCH-10, UK) at 150 MPa. The cell wall material was collected by spinning the supernatant at 20,000 g for 30 min, washing it twice with Milli-Q water, and resuspending it in SM buffer. Then, 100 μg DNase and RNase were added per gram of pellet and the sample was put on an overhead rotator for 3.5 h at room temperature. After that, the same concentration of Proteinase K was added, and the sample was again put on the overhead rotator for 2 h. After that, cell walls were extracted by boiling in 4% SDS solution for 30 min. By centrifugation at 20,000 g for 30 min, insoluble parts were recovered, and the pellet washed with Milli-Q water and centrifuged for 20 min at the same speed, repeating 5 times. The pellet was resuspended in 25 mM glycine/HCl buffer pH 2.5 and heated in a 100°C water bath for 10 min. Following centrifugation at 30,000 g for 30 min, the supernatant was discarded, and the pellet washed with and resuspended in Milli-Q water. Samples were stored in Milli-Q water at 4°C until further use for cryo-electron tomography.

Cryo-electron microscopy sample preparation and data collection

CsCl phage stocks were dialyzed against SM buffer overnight. The dialyzed sample was centrifuged at 100,000 g and 4°C for 1 h and the pellet resuspended in ~50 μl of SM buffer. The Vitrobot Mark IV (FEI, Hillsboro, Oregon) instrument was used for preparation of cryo-fixed grids. A 300-mesh, copper Quantifoil grid (Quantifoil, Germany) was first glow-discharged in air for 1 min and then

transferred to the Vitrobot's chamber that was kept at 100% relative humidity. 3.5 µl of concentrated phage stock was applied to this grid, blotted for 1 s with a blot force of 3, and plunge-frozen into a container with liquid ethane that was kept in a liquid nitrogen bath. CryoEM data were collected on a FEI Tecnai F20 200 kV FEG-TEM using either an Eagle 4 k × 4 k CCD camera (pixel size of 2.27 Å on the specimen) or a direct electron detector DE20 (pixel size of 2.35 Å on the specimen; Direct Electron, California) at the Interdisciplinary Center for Electron Microscopy (CIME) at EPFL. An additional dataset was collected on a FEI Polara using a TVIPS 4 k × 4 k CCD camera (pixel size of 2.74 Å on the specimen; TVIPS, Germany). An electron dose of ~20 e$^-$/Å^2 was used during data collection.

Cryo-electron microscopy reconstruction of phage A511 baseplate

Image processing was carried out using programs integrated in the image processing framework Scipion (de la Rosa-Trevin *et al*, 2016). Defocus estimation and correction of the effects of the microscope contrast transfer function were done with Xmipp (de la Rosa-Trevin *et al*, 2013) on micrographs binned by a factor of 2. Particles were picked manually using either EMAN boxer (Ludtke *et al*, 1999) or Xmipp particle picking on the unbinned, CTF-corrected micrographs. Particles were extracted into boxes of 300 by 300 pixels, and datasets were rescaled and processed together resulting in a total of 14,438 and 2,234 particles in pre-host attachment extended state and post-host attachment, spontaneously contracted state, respectively. Micrographs of phages on the urea-induced contracted state resulted in a total of 10,122 particles to be used for further image processing in Scipion (Table 1).

Particle datasets were subjected to alignment and classification using Relion v. 1.4 (Scheres, 2012). 2D class averages were initially calculated to remove "bad" particles. Then, 3D classification was used to establish that there was no structural heterogeneity within the datasets and to do further particle screening. 3D classes were selected based on the clear distinction of structural features such as the tail tube and fibers, as well as the helical nature of the sheath. This strategy resulted in the selection of 85% (4 classes) of the pre-host attachment dataset, and 84% (3 classes) of the post-host attachment spontaneously contracted dataset. All particles from the post-host attachment urea-induced dataset were used for further processing. 3D refinements were started from initial models generated with the help of the initial model generation procedure in EMAN through the Scipion interface. The models were low-pass-filtered to 60 Å and the refinement then carried out until convergence. After this, the resolution was improved by applying a mask during the semi-automated post-processing (Chen *et al*, 2013) resulting in a map that is sharpened and filtered at the gold standard determined resolution (Table 1).

Cryo-electron tomography data collection, tomogram reconstruction, and evaluation of the sheath contraction state of A511 in the presence of *L. monocytogenes* cell walls

Grids for cryoET were prepared as described above for cryoEM except that BSA-treated colloidal gold (10 nm particles) was either

previously applied onto the grids and air-dried or mixed with the sample for a more homogeneous gold distribution in the ice. For phage attachment, 3 µl of A511 stock was mixed with 0.5 µl of highly concentrated cell wall preparation and incubated at room temperature for either 5, 20, or 80 min. 0.5 µl of BSA-treated colloidal gold was added to the mix before plunge-freezing as indicated above.

CryoET data collection was done on a FEI Tecnai F20 200 kV FEG-TEM using an Eagle 4 k × 4 k CCD camera at CIME. Images were acquired with a pixel size of 3.82 Å on the specimen at a magnification of 29,000, which allowed us to identify phage components. A total electron dose of ~60 e$^-$/Å^2 was used in tilt series covering a wedge of −62° to 62° with an angular spacing of 2° (63 unbinned images) without visible radiation damage on the specimen. Images were collected using a 4-µm defocus. Tilt series were collected automatically using SerialEM (Mastronarde, 2005).

A total of 7 tomograms from the 5-min time point, 13 tomograms from the 20-min time point, and 11 tomograms from the 80-min time point were generated with IMOD (Kremer *et al*, 1996). The datasets were binned by factor of 2 during this process. From the reconstructed subtomograms, phage sheaths in extended, contracted, or intermediate states were segmented with IMOD and analyzed using the "analyze tubes" special option within IMOD drawing tools which is especially helpful to investigate components with variable diameter (Noske *et al*, 2008).

Expression and purification of gp105 baseplate protein

PCR-amplified fragment corresponding to gp105 was cloned into the pEE3 expression vector using the primers CTGTATTTCCAGG GATCCGCAATAGCAACATATAATGCGC and GAGTGCGGCCGCAA GCTTATAATTCCGCTACGAATCTTTC. pEE3 was derived from pET23a by introducing a TEV protease cleavage site immediately upstream of the BamHI restriction site. The resulting proteins contained the MGSSHHHHHHSSGENLYFQGS tag at the N terminus (a His-tag followed by a TEV cleavage site). The native N-formyl-methionine was replaced with the last S from the aforementioned sequence. Protein expression was performed in the 2xTY medium supplemented with ampicillin (200 µg/ml). The plasmid-carrying cells were grown to the optical density OD$_{600}$ of 0.6 and induced with IPTG to a final concentration of 0.75 mM. Cells were then incubated overnight at 18°C with rigorous shaking. The cells were pelleted at 8,000 g, resuspended in a lysis buffer (50 mM Tris–HCl, pH 8.0, 300 mM NaCl), and disrupted by sonication with a temperature maintained in the 4–16°C interval. The insoluble fraction was removed by high-speed centrifugation for 20 min at 27,000 g. The clarified cell lysate was loaded on to a 5-ml GE HisTrap FF Ni-charged column, and the protein was eluted with imidazole-containing buffer (50 mM Tris–HCl, pH 8.0; 300 mM NaCl; 200 mM Imidazole) using a step gradient. The eluted protein was dialyzed overnight into 10 mM Tris–HCl buffer, pH 8.0 at 20°C. Prior to the start of dialysis, TEV was added to the protein solution at a 1:40 w:w TEV: target protein ratio (as described in the Results and Discussion, in gp105 the His-tag is protected and was not cleaved in this procedure). The (putatively) digested protein was filtered and purified by ion-exchange chromatography (MonoQ 10/100 GL column) and 0–1 M NaCl gradient in 20 mM Tris–Cl pH 8.0 buffer. The fractions containing the target protein were pulled together. The last step of

the purification procedure was size exclusion chromatography using Superdex 75 HiLoad 16/60 column (GE Healthcare) in a buffer containing 10 mM Tris–HCl, pH 8.0, and 150 mM NaCl.

The SelenoMethionine (SeMet) derivative of gp105 was produced by expressing the protein in the 834/DE3 methionine-auxotrophic *E. coli* strain and in a medium containing SeMet instead of methionine (SelenoMethionine Medium Complete kit by Molecular Dimensions (Suffolk, UK). The purification procedure of SeMet gp105 was identical to that of the native protein.

Crystallization and data collection

SeMet-substituted gp105 was concentrated to 17 mg/ml and crystallized in two crystal forms using the hanging drop technique and two different sets of conditions. Crystal form 1 was obtained by mixing 1 μl of protein sample with 2 μl of reservoir solution of 20% PEG 6,000, 0.1 M MES pH 6.5, and 0.05 M sodium acetate. Crystal form 2 was produced with a 1:1 w/w ratio of protein: reservoir, which contained 20% PEG 6,000, 0.05 M Bis-Tris propane pH 7.5, 7% MPD and 5% t-butanol. The cryoprotectant of Crystal form 1 was a solution identical to the reservoir with an additional 30% ethylene glycol. The mother liquor of Crystal form 2 was a cryoprotectant without any additives. To prevent evaporation, these crystals were briefly immersed in oil (LV CryoOil, Mitegen, Jena Biosciences) prior to flash-freezing in liquid. All diffraction datasets were collected at the beamline PX I at the Swiss Light Source.

Crystal structure solution and refinement

The structure was solved by the single wavelength anomalous scattering technique (Wang, 1985). Se-methionine substituted crystals of Crystal form 2 diffracted to ~2.9 Å resolution and contained 8 polypeptide chains (four dimers of gp105) in the asymmetric unit of $C2_1$ unit cell. SHELXD, SHELXE (Sheldrick, 2008, 2010), and HKL2MAP (Pape & Schneider, 2004) were used to solve the Se substructure of a dataset that was collected at the Se K-edge wavelength (at the white line energy). Despite eightfold non-crystallographic averaging the electron density was poor and the resulting model was of low quality. A better dataset of Crystal form 1 that extended to 2.38 Å resolution was collected later. It belonged to the $P3_221$ space group and contained three gp105 chains (one independent dimer and one dimer on a crystallographic twofold axis) in the asymmetric unit. PHASER (McCoy *et al*, 2007) was used to solve this crystal structure by molecular replacement with the help of the Crystal form 2 gp105 model. The electron density allowed building of the complete model and several additional residues comprising the non-cleaved N-terminal His-tag. The structure was further refined with PHENIX (Adams *et al*, 2011) and autoBUSTER (Smart *et al*, 2012), rebuilt with Coot (Emsley & Cowtan, 2004) and validated with Molprobity (Chen *et al*, 2010; Table 4).

Fitting of crystal structure into the cryoEM map of the baseplate

The program COLORES (Wriggers & Chacon, 2001) from the SITUS suite (Wriggers, 2010) was utilized to carry out a search for the best fit of the gp105 dimer in all cryoEM maps. The initial automatic all-encompassing search within the complete baseplate map identified two copies of gp105 dimer per tail fiber. The third copy was placed into the map by COLORES by restricting the search to that particular location.

The T4 tail tube-baseplate core complex was fitted into the cryoEM maps by UCSF Chimera (the Fit in map option) and by Coot (Rigid body fit molecule in map option) (Pettersen *et al*, 2004; Emsley *et al*, 2010).

Table 4. Crystallographic data collection and refinement statistics.

Protein		
Crystal parameters		
Space group	C2	P3$_2$21
a, b, c (Å)	160.8, 75.1, 133.6	75.1, 75.1, 187.1
α, β, γ (°)	90.0, 102.4, 90.0	90.0, 90.0, 120.0
Resolution range (Å)[a]	49.3–2.94 (3.12–2.94)	46.8–2.38 (2.53–2.38)
R_{meas}[a]	0.083 (1.10)	0.092 (0.669)
I/σ(I)[a]	12.2 (1.14)	16.2 (2.88)
Completeness (%)[a]	94.3 (82.1)	98.9 (93.2)
Redundancy[a]	3.64 (3.50)	10.3 (9.53)

	Se SAD	Molecular Replacement
Phasing		
Number of sites	16	
Mean FOM[b]	0.599	
Refinement		
Resolution range (Å)[a]		45.05-2.38 (2.48-2.38)
R_{work}[a]		0.204 (0.2589)
R_{free}[a, c]		0.243 (0.2622)
No. of atoms		4187
Protein		4091
Heterogen		1
Solvent		95
Wilson B-factor		51.32
B-factors (Å^2)[d]		83.85
R.M.S. deviation		
Bond lengths (Å)		0.009
Bond angles (deg)		1.07
Molecules per asu	8	3
Solvent content (%)	46.75	48.36
Ramachandran plot		
Favored (%)		95.77
Allowed (%)		2.38
Outliers (%)		1.35
Clashscore		3.56 (99th percentile)
Molprobity score		2.01 (93rd percentile)
PDB ID		6HHK

[a]Values in parentheses are for the highest resolution shell.
[b]After SHELXE phasing and density modification (including model tracing).
[c]For determination of R_{free}, 5% of reflections were randomly selected before refinement.
[d]Temperature factors averaged for all atoms.

Molecular graphics

Figures 1–7, and EV2, EV3, and EV5 were prepared with the help of UCSF Chimera (Pettersen *et al*, 2004). Segmentation of cryoEM maps was carried out using the Segger plugin in UCSF Chimera (Pintilie *et al*, 2010). The tomograms were visualized with the help of IMOD (Kremer *et al*, 1996).

Data availability

CryoEM maps discussed in the paper are deposited to the EMDB database (https://www.ebi.ac.uk/pdbe/emdb/) where they were assigned the following access codes: EMD-7560, the extended A511 tail; EMD-7559, urea-treated A511 tail; EMD-7561, spontaneously contracted A511 tail. The refined crystal structure and reduced diffraction data (structure factors) of A511 gp105 were deposited to the PDB and assigned the 6HHK access code (https://www.ebi.ac.uk/pdbe/).

Expanded View for this article is available online.

Author contributions

RG-F performed cryoEM and cryoET of A511 and calculated all A511 reconstructions; RG-F, MH and JK purified the A511 bacteriophage and *Listeria* cell walls; MH and JK cloned and expressed various A511 baseplate proteins and their fragments; NMIT, RG-F, and PGL determined the crystal structure of gp105; NMIT performed the crystallographic refinement of gp105; MMS created the construct for purification of gp105, purified, and crystallized the protein; SN performed cryoEM and image reconstruction of CBA120 bacteriophage; SN, JMO, and TI assisted RG-F with microscopy and image processing; RG-F and PGL wrote the first draft of the paper and created the figures; all authors read and edited the paper. PGL, MJL, TI, and JK coordinated the joint project and provided funding.

Conflict of interest

The authors declare that they have no conflict of interest.

References

Adams PD, Afonine PV, Bunkoczi G, Chen VB, Echols N, Headd JJ, Hung LW, Jain S, Kapral GJ, Grosse Kunstleve RW, McCoy AJ, Moriarty NW, Oeffner RD, Read RJ, Richardson DC, Richardson JS, Terwilliger TC, Zwart PH (2011) The Phenix software for automated determination of macromolecular structures. *Methods* 55: 94–106

Aksyuk AA, Leiman PG, Kurochkina LP, Shneider MM, Kostyuchenko VA, Mesyanzhinov VV, Rossmann MG (2009) The tail sheath structure of bacteriophage T4: a molecular machine for infecting bacteria. *EMBO J* 28: 821–829

Alva V, Nam SZ, Soding J, Lupas AN (2016) The MPI bioinformatics Toolkit as an integrative platform for advanced protein sequence and structure analysis. *Nucleic Acids Res* 44: W410–W415

Benz WC, Goldberg EB (1973) Interactions between modified phage T4 particles and spheroplasts. *Virology* 53: 225–235

Brackmann M, Wang J, Basler M (2018) Type VI secretion system sheath inter-subunit interactions modulate its contraction. *EMBO Rep* 19: 225–233

Browning C, Shneider MM, Bowman VD, Schwarzer D, Leiman PG (2012) Phage pierces the host cell membrane with the iron-loaded spike. *Structure* 20: 326–339

Buth SA, Shneider MM, Scholl D, Leiman PG (2018) Structure and analysis of R1 and R2 pyocin receptor-binding fibers. *Viruses* 10: E427

Buttner CR, Wu Y, Maxwell KL, Davidson AR (2016) Baseplate assembly of phage Mu: defining the conserved core components of contractile-tailed phages and related bacterial systems. *Proc Natl Acad Sci USA* 113: 10174–10179

Chen VB, Arendall WB III, Headd JJ, Keedy DA, Immormino RM, Kapral GJ, Murray LW, Richardson JS, Richardson DC (2010) MolProbity: all-atom structure validation for macromolecular crystallography. *Acta Crystallogr D Biol Crystallogr* 66: 12–21

Chen S, McMullan G, Faruqi AR, Murshudov GN, Short JM, Scheres SH, Henderson R (2013) High-resolution noise substitution to measure overfitting and validate resolution in 3D structure determination by single particle electron cryomicroscopy. *Ultramicroscopy* 135: 24–35

Cheng Y, Grigorieff N, Penczek PA, Walz T (2015) A primer to single-particle cryo-electron microscopy. *Cell* 161: 438–449

Chibani-Chennoufi S, Dillmann ML, Marvin-Guy L, Rami-Shojaei S, Brussow H (2004) Lactobacillus plantarum bacteriophage LP65: a new member of the SPO1-like genus of the family Myoviridae. *J Bacteriol* 186: 7069–7083

Dickson RC (1973) Assembly of bacteriophage T4 tail fibers. IV. Subunit composition of tail fibers and fiber precursors. *J Mol Biol* 79: 633–647

Donelli G, Guglielmi F, Paoletti L (1972) Structure and physico-chemical properties of bacteriophage G. I. Arrangement of protein subunits and contraction process of tail sheath. *J Mol Biol* 71: 113–125

Eiserling FA (1967) The structure of Bacillus subtilis bacteriophage PBS 1. *J Ultrastruct Res* 17: 342–347

Emsley P, Cowtan K (2004) Coot: model-building tools for molecular graphics. *Acta Crystallogr D Biol Crystallogr* 60: 2126–2132

Emsley P, Lohkamp B, Scott WG, Cowtan K (2010) Features and development of Coot. *Acta Crystallogr D Biol Crystallogr* 66: 486–501

Fokine A, Zhang Z, Kanamaru S, Bowman VD, Aksyuk AA, Arisaka F, Rao VB, Rossmann MG (2013) The molecular architecture of the bacteriophage T4 neck. *J Mol Biol* 425: 1731–1744

Ge P, Scholl D, Leiman PG, Yu X, Miller JF, Zhou ZH (2015) Atomic structures of a bactericidal contractile nanotube in its pre- and postcontraction states. *Nat Struct Mol Biol* 22: 377–382

Guenther S, Huwyler D, Richard S, Loessner MJ (2009) Virulent bacteriophage for efficient biocontrol of Listeria monocytogenes in ready-to-eat foods. *Appl Environ Microbiol* 75: 93–100

Habann M, Leiman PG, Vandersteegen K, Van den Bossche A, Lavigne R, Shneider MM, Bielmann R, Eugster MR, Loessner MJ, Klumpp J (2014) Listeria phage A511, a model for the contractile tail machineries of SPO1-related bacteriophages. *Mol Microbiol* 92: 84–99

Hagens S, de Wouters T, Vollenweider P, Loessner MJ (2011) Reporter bacteriophage A511: celB transduces a hyperthermostable glycosidase from Pyrococcus furiosus for rapid and simple detection of viable Listeria cells. *Bacteriophage* 1: 143–151

Hu B, Margolin W, Molineux IJ, Liu J (2015) Structural remodeling of bacteriophage T4 and host membranes during infection initiation. *Proc Natl Acad Sci USA* 112: E4919–E4928

Kanamaru S, Leiman PG, Kostyuchenko VA, Chipman PR, Mesyanzhinov VV, Arisaka F, Rossmann MG (2002) Structure of the cell-puncturing device of bacteriophage T4. *Nature* 415: 553–557

Kazmierczak Z, Gorski A, Dabrowska K (2014) Facing antibiotic resistance: *Staphylococcus aureus* phages as a medical tool. *Viruses* 6: 2551–2570

Klumpp J, Dorscht J, Lurz R, Bielmann R, Wieland M, Zimmer M, Calendar R, Loessner MJ (2008) The terminally redundant, nonpermuted genome of Listeria bacteriophage A511: a model for the SPO1-like myoviruses of gram-positive bacteria. *J Bacteriol* 190: 5753–5765

Klumpp J, Lavigne R, Loessner MJ, Ackermann HW (2010) The SPO1-related bacteriophages. *Arch Virol* 155: 1547–1561

Koc C, Xia G, Kuhner P, Spinelli S, Roussel A, Cambillau C, Stehle T (2016) Structure of the host-recognition device of *Staphylococcus aureus* phage varphi11. *Sci Rep* 6: 27581

Kostyuchenko V, Leiman P, Chipman P, Kanamaru S, van Raaij M, Arisaka F, Mesyanzhinov V, Rossmann M (2003) Three-dimensional structure of bacteriophage T4 baseplate. *Nat Struct Biol* 10: 688–693

Kostyuchenko VA, Chipman PR, Leiman PG, Arisaka F, Mesyanzhinov VV, Rossmann MG (2005) The tail structure of bacteriophage T4 and its mechanism of contraction. *Nat Struct Mol Biol* 12: 810–813

Kremer JR, Mastronarde DN, McIntosh JR (1996) Computer visualization of three-dimensional image data using IMOD. *J Struct Biol* 116: 71–76

Kudryashev M, Wang RY, Brackmann M, Scherer S, Maier T, Baker D, DiMaio F, Stahlberg H, Egelman EH, Basler M (2015) Structure of the type VI secretion system contractile sheath. *Cell* 160: 952–962

Kwan T, Liu J, DuBow M, Gros P, Pelletier J (2005) The complete genomes and proteomes of 27 *Staphylococcus aureus* bacteriophages. *Proc Natl Acad Sci USA* 102: 5174–5179

Leiman PG, Shneider MM, Kostyuchenko VA, Chipman PR, Mesyanzhinov VV, Rossmann MG (2003) Structure and location of gene product 8 in the bacteriophage T4 baseplate. *J Mol Biol* 328: 821–833

Leiman PG, Chipman PR, Kostyuchenko VA, Mesyanzhinov VV, Rossmann MG (2004) Three-dimensional rearrangement of proteins in the tail of bacteriophage T4 on infection of its host. *Cell* 118: 419–429

Leiman PG, Shneider MM (2012) Contractile tail machines of bacteriophages. *Adv Exp Med Biol* 726: 93–114

Loessner MJ (1991) Improved procedure for bacteriophage typing of Listeria strains and evaluation of new phages. *Appl Environ Microbiol* 57: 882–884

Loessner MJ, Scherer S (1995) Organization and transcriptional analysis of the Listeria phage A511 late gene region comprising the major capsid and tail sheath protein genes cps and tsh. *J Bacteriol* 177: 6601–6609

Loessner MJ, Rees CE, Stewart GS, Scherer S (1996) Construction of luciferase reporter bacteriophage A511: luxAB for rapid and sensitive detection of viable Listeria cells. *Appl Environ Microbiol* 62: 1133–1140

Ludtke SJ, Baldwin PR, Chiu W (1999) EMAN: semiautomated software for high-resolution single-particle reconstructions. *J Struct Biol* 128: 82–97

Mastronarde DN (2005) Automated electron microscope tomography using robust prediction of specimen movements. *J Struct Biol* 152: 36–51

Maxwell KL, Fatehi Hassanabad M, Chang T, Paul VD, Pirani N, Bona D, Edwards AM, Davidson AR (2013) Structural and functional studies of gpX of *Escherichia coli* phage P2 reveal a widespread role for LysM domains in the baseplates of contractile-tailed phages. *J Bacteriol* 195: 5461–5468

McCoy AJ, Grosse-Kunstleve RW, Adams PD, Winn MD, Storoni LC, Read RJ (2007) Phaser crystallographic software. *J Appl Crystallogr* 40: 658–674

van der Mee-Marquet N, Loessner M, Audurier A (1997) Evaluation of seven experimental phages for inclusion in the international phage set for the epidemiological typing of Listeria monocytogenes. *Appl Environ Microbiol* 63: 3374–3377

Miao H, Jia Y, Xie S, Wang X, Zhao J, Chu Y, Zhou Z, Shi Z, Song X, Li L (2014) Structural insights into the C1q domain of Caprin-2 in canonical Wnt signaling. *J Biol Chem* 289: 34104–34113

Moody MF (1973) Sheath of bacteriophage T4. 3. Contraction mechanism deduced from partially contracted sheaths. *J Mol Biol* 80: 613–635

Noske AB, Costin AJ, Morgan GP, Marsh BJ (2008) Expedited approaches to whole cell electron tomography and organelle mark-up *in situ* in high-pressure frozen pancreatic islets. *J Struct Biol* 161: 298–313

Novacek J, Siborova M, Benesik M, Pantucek R, Doskar J, Plevka P (2016) Structure and genome release of Twort-like Myoviridae phage with a double-layered baseplate. *Proc Natl Acad Sci USA* 113: 9351–9356

Pape T, Schneider TR (2004) HKL2MAP: a graphical user interface for macromolecular phasing with SHELX programs. *J Appl Crystallogr* 37: 843–844

Pettersen EF, Goddard TD, Huang CC, Couch GS, Greenblatt DM, Meng EC, Ferrin TE (2004) UCSF Chimera–a visualization system for exploratory research and analysis. *J Comput Chem* 25: 1605–1612

Pintilie GD, Zhang J, Goddard TD, Chiu W, Gossard DC (2010) Quantitative analysis of cryo-EM density map segmentation by watershed and scale-space filtering, and fitting of structures by alignment to regions. *J Struct Biol* 170: 427–438

van Raaij MJ, Schoehn G, Burda MR, Miller S (2001) Crystal structure of a heat and protease-stable part of the bacteriophage T4 short tail fibre. *J Mol Biol* 314: 1137–1146

Rice LM, Earnest TN, Brunger AT (2000) Single-wavelength anomalous diffraction phasing revisited. *Acta Crystallogr D Biol Crystallogr* 56: 1413–1420

de la Rosa-Trevin JM, Oton J, Marabini R, Zaldivar A, Vargas J, Carazo JM, Sorzano CO (2013) Xmipp 3.0: an improved software suite for image processing in electron microscopy. *J Struct Biol* 184: 321–328

de la Rosa-Trevin JM, Quintana A, Del Cano L, Zaldivar A, Foche I, Gutierrez J, Gomez-Blanco J, Burguet-Castell J, Cuenca-Alba J, Abrishami V, Vargas J, Oton J, Sharov G, Vilas JL, Navas J, Conesa P, Kazemi M, Marabini R, Sorzano CO, Carazo JM (2016) Scipion: a software framework toward integration, reproducibility and validation in 3D electron microscopy. *J Struct Biol* 195: 93–99

Rossmann MG, Blow DM (1962) The detection of sub-units within the crystallographic asymmetric unit. *Acta Crystallogr A* 15: 24–31

Scheres SH (2012) RELION: implementation of a Bayesian approach to cryo-EM structure determination. *J Struct Biol* 180: 519–530

Schwarzer D, Buettner FF, Browning C, Nazarov S, Rabsch W, Bethe A, Oberbeck A, Bowman VD, Stummeyer K, Muhlenhoff M, Leiman PG, Gerardy-Schahn R (2012) A multivalent adsorption apparatus explains the broad host range of phage phi92: a comprehensive genomic and structural analysis. *J Virol* 86: 10384–10398

Sciara G, Bebeacua C, Bron P, Tremblay D, Ortiz-Lombardia M, Lichiere J, van Heel M, Campanacci V, Moineau S, Cambillau C (2010) Structure of lactococcal phage p2 baseplate and its mechanism of activation. *Proc Natl Acad Sci USA* 107: 6852–6857

Sheldrick GM (2008) A short history of SHELX. *Acta Crystallogr A* 64: 112–122

Sheldrick GM (2010) Experimental phasing with SHELXC/D/E: combining chain tracing with density modification. *Acta Crystallogr D Biol Crystallogr* 66: 479–485

Simon LD, Anderson TF (1967a) The infection of *Escherichia coli* by T2 and T4 bacteriophages as seen in the electron microscope. I. Attachment and penetration. *Virology* 32: 279–297

Simon LD, Anderson TF (1967b) The infection of *Escherichia coli* by T2 and T4 bacteriophages as seen in the electron microscope. II. Structure and function of the baseplate. *Virology* 32: 298–305

Smart OS, Womack TO, Flensburg C, Keller P, Paciorek W, Sharff A, Vonrhein C, Bricogne G (2012) Exploiting structure similarity in refinement: automated NCS and target-structure restraints in BUSTER. *Acta Crystallogr D Biol Crystallogr* 68: 368–380

Soding J, Biegert A, Lupas AN (2005) The HHpred interactive server for protein homology detection and structure prediction. *Nucleic Acids Res* 33: W244–W248

Squeglia F, Ruggiero A, Romano M, Vitagliano L, Berisio R (2014) Mutational and structural study of RipA, a key enzyme in Mycobacterium tuberculosis cell division: evidence for the L-to-D inversion of configuration of the catalytic cysteine. *Acta Crystallogr D Biol Crystallogr* 70: 2295–2300

Stewart CR, Casjens SR, Cresawn SG, Houtz JM, Smith AL, Ford ME, Peebles CL, Hatfull GF, Hendrix RW, Huang WM, Pedulla ML (2009) The genome of Bacillus subtilis bacteriophage SPO1. *J Mol Biol* 388: 48–70

Taylor NM, Prokhorov NS, Guerrero-Ferreira RC, Shneider MM, Browning C, Goldie KN, Stahlberg H, Leiman PG (2016) Structure of the T4 baseplate and its function in triggering sheath contraction. *Nature* 533: 346–352

Taylor NMI, van Raaij MJ, Leiman PG (2018) Contractile injection systems of bacteriophages and related systems. *Mol Microbiol* 108: 6–15

Vandersteegen K, Mattheus W, Ceyssens PJ, Bilocq F, De Vos D, Pirnay JP, Noben JP, Merabishvili M, Lipinska U, Hermans K, Lavigne R (2011) Microbiological and molecular assessment of bacteriophage ISP for the control of *Staphylococcus aureus*. *PLoS One* 6: e24418

Vettiger A, Basler M (2016) Type VI secretion system substrates are transferred and reused among sister cells. *Cell* 167: 99–110.e12

Wang BC (1985) Resolution of phase ambiguity in macromolecular crystallography. *Methods Enzymol* 115: 90–112

Wendlinger G, Loessner MJ, Scherer S (1996) Bacteriophage receptors on Listeria monocytogenes cells are the N-acetylglucosamine and rhamnose substituents of teichoic acids or the peptidoglycan itself. *Microbiology* 142 (Pt 4): 985–992

Williams SR, Gebhart D, Martin DW, Scholl D (2008) Retargeting R-type pyocins to generate novel bactericidal protein complexes. *Appl Environ Microbiol* 74: 3868–3876

Wriggers W, Chacon P (2001) Modeling tricks and fitting techniques for multiresolution structures. *Structure* 9: 779–788

Wriggers W (2010) Using Situs for the integration of multi-resolution structures. *Biophys Rev* 2: 21–27

Zink R, Loessner MJ (1992) Classification of virulent and temperate bacteriophages of Listeria spp. on the basis of morphology and protein analysis. *Appl Environ Microbiol* 58: 296–302